# Decoupling Algorithm of Six-Axis Acceleration Sensing Mechanisms

ZHANG Yuanwei, YOU Jingjing\*, ZHANG Xianzhu, SHI Haofei

College of Mechanical and Electrical Engineering, Nanjing Forest University, Nanjing 210037, P. R. China

(Received 23 May 2025; revised 23 July 2025; accepted 10 August 2025)

**Abstract:** To address the issues of low solving efficiency and poor decoupling accuracy in existing six-axis acceleration decoupling algorithms, a new decoupling algorithm is proposed along with a corresponding auto-compensation algorithm. Firstly, based on Kane's method, the dynamics model of the six-axis acceleration sensing mechanism is formed to determine the relationship between accelerations and branch forces. Then, with the trapezoidal rule, a solution algorithm for the dynamics model is developed. The virtual prototype tests show that the computation of this algorithm is five times more efficient than that of the ADAMS core algorithm. Besides, this solution algorithm is applied to the "12-6" configuration and "9-3" configuration. The results show that the efficiency of the former is nearly 3.3 times that of the latter. Finally, based on vibration theory, an auto-compensation algorithm for the solution algorithm is established. Virtual prototype tests indicate that with 40% noise interference, the auto-compensation algorithm achieves misjudgement rate and omission rate of only 4.0% and 4.5%, respectively, and the errors in the solving process converge.

Key words: six-axis acceleration sensing mechanism; Kane's method; trapezoidal rule; auto-compensation

**CLC number:** TH825 **Document code:** A **Article ID:** 1005-1120(2025)S-0141-09

### 0 Introduction

With the further advancement of Industry 4.0, manipulators have become widely used in the manufacturing industry. The control of manipulators often relies on feedback from end-effectors' sensors, and the information measured by these sensors usually needs to include the position and pose of the robot's end-effector. Additionally, during movement and processing, manipulators inevitably experience vibrations, which can reduce processing accuracy. However, feedback from end-effectors' sensors can effectively suppress these vibrations. Therefore, accurately measuring the six-axis acceleration information at end-effectors is an urgent issue that needs to be addressed in the field of manipulators.

Traditional six-axis acceleration measurement methods typically use a combination of accelerometers and gyroscopes to measure the spacecraft's three-axis linear acceleration and three-axis angular acceleration and then integrate to obtain the pose information. However, gyroscopes are easily affected by environmental factors such as lighting and temperature, making this method less effective [3-7]. To address this, some researchers have proposed gyroscope-free six-axis acceleration measurement schemes. The most common gyroscope-free methods are the multi-inertial mass scheme and the single-inertial mass scheme. The multi-inertial mass scheme also faces high installation precision requirements and issues such as significant lever-arm effects and cross-sensitivity effects, making its practicality lower<sup>[8]</sup>. In the single-inertial mass scheme, the accelerometer's structure is relatively complex, leading to coupling between six-axis accelerations. Researchers like You et al. [9] have proposed a decoupling algorithm for six-axis accelerometer, but this algorithm has low solution efficiency and cannot meet the real-time computation requirements for acceleration measurement. In 2017, You et al. [10] proposed a new decoupling algorithm which had high

<sup>\*</sup>Corresponding author, E-mail address: youjingjing251010@njfu.edu.cn.

solution efficiency, but there was an error accumulation process in the solution process. It is crucial for the acceleration decoupling to establish a viable dynamic model of the system. Newton-Euler method<sup>[10]</sup> suffers from insufficient accuracy due to its neglect of relative motions, and Hamilton's method<sup>[9]</sup> appears inefficiency with 14 variables introduced. Kane's method strikes a great balance between these approaches, demonstrating significant practical potential for acceleration decoupling.

Based on this, this paper establishes the dynamic model of the six-axis acceleration sensing mechanism using Kane's method and proposes a new solution algorithm based on the trapezoidal rule. An auto-compensation algorithm is developed based on vibration theory, which offers high efficiency and accuracy, and its effectiveness and accuracy are validated through simulation.

## 1 Description of Mechanism

Fig.1 shows the six-axis accelerometer. In this mechanism, the flexible spherical hinges are located at the midpoints of the inertial mass's edges. When an external acceleration is applied to the accelerometer, the inertial mass experiences inertial forces, causing relative displacement between the inertial mass and the pedestal, and generating axial forces in all the branches between the inertial mass and the pedestal. Using the piezoelectric ceramics arranged on the branches, the axial forces are measured; further decoupling of the measured data allows for the determination of the six-axis acceleration of the pedestal.

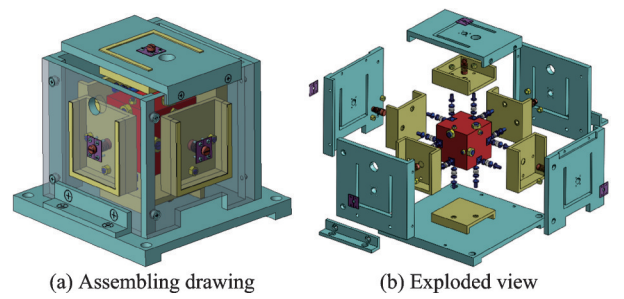


Fig.1 Six-axis accelerometer

## 2 Dynamic Analysis

The core component of a six-axis accelerome-

ter is the sensing mechanism. The inputs of the sensing mechanism consist of six independent components of the pedestal's acceleration, while the outputs comprise the axial forces in 12 branches. Each input affects all outputs, making the accelerometer a nonlinear and strongly coupled system with multiple inputs and outputs. The process of deriving outputs from inputs by constructing the system's dynamic equations is known as "forward dynamics solution" while deriving inputs from outputs is referred to as "inverse dynamics solution" or "decoupling".

According to Ref.[10], in the inverse dynamics analysis of the mechanism, the relative displacement between the inertial mass and the pedestal can be neglected. Coordinate systems  $\{O\}$  and  $\{Q\}$  are established on the ground and the inertial mass, respectively, with the origins of both coordinate systems initially coinciding with the geometrical centre of the inertial mass. The schematic diagram of the sensing mechanism and the positions of the coordinate systems are shown in Fig.2.

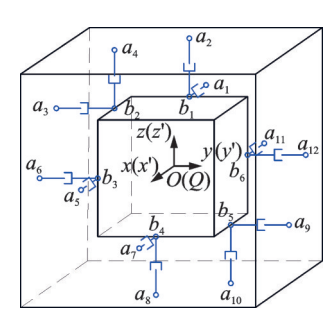


Fig.2 Schematic diagram of six-axis acceleration sensing mechanism

Common methods for establishing a dynamic model include the Newton-Euler method, the second Lagrange equation method, Kane's method and Hamilton's method. Among these, Kane's method has the least computational effort and highest efficiency, making it suitable for dynamic analysis of closed-loop mechanisms. The expression for Kane's equation is

$$K_i + K_i^* = 0$$
  $j = 1, 2, 3, 4, 5, 6$  (1)

where  $K_j$  and  $K_j^*$  represent the generalized active force and generalized inertial force corresponding to the *j*th generalized velocity, respectively.

Upon analysis, the inertial mass of the sensing mechanism is acted upon branch forces and gravity.

Using simplification of the space force system, all external forces can be reduced to a resultant force and a resultant moment placed on the inertial mass. Therefore, the generalized form of Kane's equations can be applied.

 $R_{\rm C} \cdot v_{\rm Cj} + L_{\rm C} \cdot \omega_{\rm Cj} + R_{\rm C}^* \cdot v_{\rm Cj} + L_{\rm C}^* \cdot \omega_{\rm Cj} = 0$  (2) where  $R_{\rm C}$ ,  $L_{\rm C}$ ,  $R_{\rm C}^*$ , and  $L_{\rm C}^*$  represent the resultant force, resultant moment, inertial force, and inertial moment, respectively, placed on the geometrical centre of the inertial mass; and  $v_{\rm Cj}$  and  $\omega_{\rm Cj}$  the partial linear velocity and partial angular velocity corresponding to the *j*th generalized velocity, respectively.

In the coordinate system  $\{O\}$ , the linear velocity and angular velocity of the inertial mass's geometrical centre are given

$$\begin{cases} v_{c} = (\dot{x}, \dot{y}, \dot{z})^{T} = \dot{x}i + \dot{y}j + \dot{z}k \\ \omega_{c} = \omega_{x}i + \omega_{y}j + \omega_{z}k \end{cases}$$
(3)

where  $\dot{x}$ ,  $\dot{y}$ ,  $\dot{z}$ ,  $\omega_x$ ,  $\omega_y$ , and  $\omega_z$  denote the linear velocities and angular velocities of the inertial mass in coordinate system  $\{O\}$ . Taking these six quantities as the generalized velocities for the system, the corresponding partial linear velocities and partial angular velocities are listed in Table 1.

Table 1 Analytical equations of partial velocities

$\boldsymbol{v}_{\mathrm{C1}}$	$\boldsymbol{v}_{\mathrm{C2}}$	$\boldsymbol{v}_{\mathrm{C3}}$	$\boldsymbol{v}_{\mathrm{C4}}$	$\boldsymbol{v}_{\mathrm{C5}}$	$\boldsymbol{v}_{\mathrm{C6}}$	$\omega_{\rm Cl}$	$\boldsymbol{\omega}_{\mathrm{C2}}$	$\omega_{C3}$	$\omega_{C4}$	$\omega_{C5}$	$\omega_{C6}$	
i	j	k	0	0	0	0	0	0	i	j	k	

Except for gravity, the direction of the branch forces placed on the inertial mass remains unchanged in the coordinate system  $\{Q\}$ . Therefore, the simplified resultant force and resultant moment can be expressed as

$$\begin{cases} \mathbf{R}_{C} = \sum_{i=1}^{12} f_{i} \mathbf{e}_{i} + Mg(0,0,-1) = \\ \sum_{i=1}^{12} f_{i} \mathbf{R}_{3 \times 3} \mathbf{e}'_{i} + Mg(0,0,-1) \\ L_{C} = \sum_{j=1}^{6} \left( \mathbf{b}_{j} \times \sum_{i=2j-1}^{2j} f_{i} \mathbf{e}_{i} \right) = \\ \sum_{j=1}^{6} \left( \mathbf{R}_{3 \times 3} \mathbf{b}'_{j} \times \sum_{i=2j-1}^{2j} f_{i} \mathbf{R}_{3 \times 3} \mathbf{e}'_{i} \right) \end{cases}$$

$$(4)$$

where  $R_{3\times3}$  denotes the rotation matrix describing the relative rotation between the two coordinate systems; M the inertial mass;  $f_i$  the force exerted by the ith branch on the mass;  $e_i$  the direction vector of the ith branch in  $\{O\}$ ;  $e'_i$  the direction vector of the

ith branch in  $\{Q\}$ ; and  $b_j$  the position vector of the jth moving spherical hinge in  $\{O\}$ , and

$$(e_1'-e_{12}')=$$

$$(\boldsymbol{b}_{1}^{\prime}-\boldsymbol{b}_{6}^{\prime}) = \begin{pmatrix} -1 & 0 & 1 & 1 & 0 & -1 \\ 0 & -1 & -1 & 0 & 1 & 1 \\ 1 & 1 & 0 & -1 & -1 & 0 \end{pmatrix}$$
(6)

The inertial force and the inertial moment are

$$R_{\rm C}^* = -Ma_{\rm C} \tag{7}$$

$$L_{\mathrm{C}}^* = -(I_{3\times3}\dot{\boldsymbol{\omega}} - \boldsymbol{\omega} \times I_{3\times3}\boldsymbol{\omega}) \tag{8}$$

where  $I_{3\times3}$  represents the rotational inertia of the inertial mass in  $\{O\}$ ;  $a_{\rm C}$  the linear acceleration at the geometrical centre of the inertial mass, and

$$I_{3\times3} = R_{3\times3}I_{3\times3}^{\prime}R_{3\times3}^{\mathrm{T}} = \left(\frac{2}{3}Mn^{2} - \frac{2}{3}Mn^{2} - \frac{2}{3}Mn^{2} - \frac{2}{3}Mn^{2}\right)R_{3\times3}^{\mathrm{T}}$$
(9)

Combining Table 1 and substituting Eqs.(4—9) into Eq.(2), the dynamic equation is obtained as follows

$$\begin{cases}
D_{1} \cdot \mathbf{i} - Ma_{C} \cdot \mathbf{i} = 0 \\
D_{1} \cdot \mathbf{j} - Ma_{C} \cdot \mathbf{j} = 0 \\
D_{1} \cdot \mathbf{k} - Ma_{C} \cdot \mathbf{k} = 0 \\
D_{2} \cdot \mathbf{i} + D_{3} \cdot \mathbf{i} = 0 \\
D_{2} \cdot \mathbf{j} + D_{3} \cdot \mathbf{j} = 0 \\
D_{2} \cdot \mathbf{k} + D_{3} \cdot \mathbf{k} = 0
\end{cases} (10)$$

where

$$D_{1} = \sum_{i=1}^{12} f_{i} \mathbf{R}_{3 \times 3} \mathbf{e}'_{i} + Mg(0,0,-1)^{T}$$
 (11)

$$D_2 = \sum_{i=1}^{6} \left( \boldsymbol{R}_{3 \times 3} \boldsymbol{b}_j' \times \sum_{i=2i-1}^{2j} f_i \boldsymbol{R}_{3 \times 3} \boldsymbol{e}_i' \right)$$
 (12)

$$D_{3} = -R_{3\times3}I'_{3\times3}R^{\mathsf{T}}_{3\times3}\dot{\boldsymbol{\omega}} - \boldsymbol{\omega} \times R_{3\times3}I'_{3\times3}R^{\mathsf{T}}_{3\times3}\boldsymbol{\omega}$$

$$\tag{13}$$

## 3 Dynamic Solution

## 3. 1 Solution algorithm

Considering that quaternions are used to describe the rotation of three-dimensional objects, and the rotation matrix is a  $4\times4$  matrix formed by qua-

ternions, other vectors also need to be extended. The dynamic equation is expanded and simplified as follows

$$\ddot{x}_{\text{C}} = \frac{1}{M} \sum_{i=1}^{12} f_{i} R_{4 \times 4} E_{i}^{\prime} \cdot I$$

$$\ddot{y}_{\text{C}} = \frac{1}{M} \sum_{i=1}^{12} f_{i} R_{4 \times 4} E_{i}^{\prime} \cdot I$$

$$\ddot{z}_{\text{C}} = \frac{1}{M} \sum_{i=1}^{12} f_{i} R_{4 \times 4} E_{i}^{\prime} \cdot K - Mg$$

$$\dot{W} = R_{4 \times 4} (I_{4 \times 4}^{\prime\prime})^{-1} R_{4 \times 4}^{\text{T}} \left[ \sum_{j=1}^{6} (R_{4 \times 4} B_{j}^{\prime} \times I_{4 \times 4}^{\text{T}} I_{$$

where  $E'_i$ ,  $B'_j$ , W, I, J, and K are extended vectors of  $e'_i$ ,  $b'_j$ ,  $\omega$ , i, j, and k in four-dimensional space; and  $R_{4\times 4}$  is the extension of  $R_{3\times 3}$ .

Eq.(14) describes the relationship between accelerations and branch forces, where only W and  $R_{4\times4}$  are unknowns. Solving for these two unknowns will yield the decoupling equations for six-axis acceleration.

Define an arbitrary four-dimensional vector  $\boldsymbol{S}$ , along with its pre-matrix and post-matrix

$$S = (s_1, s_2, s_3, s_0)^{\mathrm{T}} \tag{15}$$

$$\overset{+}{S} = \begin{pmatrix}
s_0 & -s_3 & s_2 & s_1 \\
s_3 & s_0 & -s_1 & s_2 \\
-s_2 & s_1 & s_0 & s_3 \\
-s_1 & -s_2 & -s_3 & s_0
\end{pmatrix}$$
(16)

$$\vec{S} = \begin{pmatrix}
s_0 & s_3 & -s_2 & s_1 \\
-s_3 & s_0 & s_1 & s_2 \\
s_2 & -s_1 & s_0 & s_3 \\
-s_4 & -s_5 & -s_5 & s_5
\end{pmatrix}$$
(17)

The quaternion vector  $\boldsymbol{\Lambda}$  is four-dimensional. Thus, according to Ref.[10], the relationship between the four-dimensional rotation matrix  $\boldsymbol{R}_{4\times4}$  and the quaternion vector  $\boldsymbol{\Lambda}$  is given by

$$\boldsymbol{R}_{4\times4} = \left(\boldsymbol{\bar{\Lambda}}\right)^{\mathrm{T}} \boldsymbol{\bar{\Lambda}} \tag{18}$$

Besides, the pre- and post-matrix satisfy the following properties

$$\stackrel{+}{\mathbf{S}} \stackrel{-}{\mathbf{S}} = \stackrel{-}{\mathbf{S}} \stackrel{+}{\mathbf{S}}$$

$$\stackrel{+}{\mathbf{\Lambda}} \left( \stackrel{+}{\mathbf{\Lambda}} \right)^{\mathsf{T}} = \left( \stackrel{+}{\mathbf{\Lambda}} \right)^{\mathsf{T}} \stackrel{+}{\mathbf{\Lambda}} = \stackrel{-}{\mathbf{\Lambda}} \left( \stackrel{-}{\mathbf{\Lambda}} \right)^{\mathsf{T}} = \left( \stackrel{-}{\mathbf{\Lambda}} \right)^{\mathsf{T}} \stackrel{-}{\mathbf{\Lambda}} = E_{4}$$
(20)

$$\stackrel{+}{\boldsymbol{\Lambda}} \stackrel{-}{\boldsymbol{S}} \left( \stackrel{+}{\boldsymbol{\Lambda}} \right)^{\mathrm{T}} = \stackrel{-}{\boldsymbol{S}}$$
 (21)

Eqs.(19—21) is defined as "property 1" "property 2" and "property 3", respectively. In the case of three dimensions, the derivative of  $\mathbf{R}_{3\times3}$  is represented as

$$\dot{R}_{3\times3} = \hat{\omega} R_{3\times3} \tag{22}$$

where  $\hat{\boldsymbol{\omega}}$  is the anti-symmetric matrix of vector  $\boldsymbol{\omega}$ . Expanding the Eq.(22) into four-dimensional space, it is written as

$$\dot{R}_{4\times4} = \hat{W}R_{4\times4} \tag{23}$$

where  $\hat{W}$  can be presented as

$$\hat{\mathbf{W}} = \frac{\mathbf{W} - \mathbf{W}}{2} \tag{24}$$

Substituting Eqs.(18, 24) into Eq.(23), it is written as

$$2\left(\bar{\dot{\boldsymbol{\Lambda}}}\right)^{\mathrm{T}}\boldsymbol{\dot{\Lambda}} + 2\left(\bar{\boldsymbol{\Lambda}}\right)^{\mathrm{T}}\dot{\boldsymbol{\dot{\Lambda}}} = \boldsymbol{\dot{W}}\left(\bar{\boldsymbol{\Lambda}}\right)^{\mathrm{T}}\boldsymbol{\dot{\Lambda}} - \bar{\boldsymbol{W}}\left(\bar{\boldsymbol{\Lambda}}\right)^{\mathrm{T}}\boldsymbol{\dot{\Lambda}}$$
(25)

Eq.(25) with property 1, property 2 and property 3 is simplified as

$$2\left(\bar{\dot{\boldsymbol{\Lambda}}}\right)^{\mathrm{T}}\bar{\boldsymbol{\Lambda}} + 2\dot{\dot{\boldsymbol{\Lambda}}}\left(\bar{\boldsymbol{\Lambda}}\right)^{\mathrm{T}} = \bar{\boldsymbol{W}} - \bar{\boldsymbol{W}}$$
 (26)

Eq.(26) with property 2 is simplified as

$$\dot{\mathbf{\Lambda}} = \frac{1}{2} \stackrel{+}{\mathbf{\Lambda}} \mathbf{W}' \tag{27}$$

The angular velocity projected in the inertial mass coordinate  $\omega'$  is defined as auxiliary angular velocity and it is expanded to a four-dimensional vector  $\mathbf{W}'$ . The relationship between  $\mathbf{W}$  and  $\mathbf{W}'$  is

$$W = R_{4 \times 4} W' \tag{28}$$

Differentiating both sides of Eq.(28) gives

$$\dot{W} = \hat{W}R_{4\times4}W' + R_{4\times4}\dot{W}' = R_{4\times4}\dot{W}' \qquad (29)$$

Substituting Eq.(29) into Eq.(14) obtains

$$\dot{W}' = -(I'_{4\times 4})^{-1} \sum_{i=1}^{6} \left( B'_{i} \times \sum_{i=2i-1}^{2j} f_{i} E'_{i} \right) = V \quad (30)$$

Using the trapezoidal rule to solve Eqs. (27, 30), we have

$$W'_{(N)} = W'_{(N-1)} + \frac{h}{2}(V_{(N-1)} + V_{(N)})$$
 (31)

$$\mathbf{\Lambda}_{(N)} = \mathbf{\Lambda}_{(N-1)} + \frac{h}{4} \frac{h}{\mathbf{\Lambda}}_{(N-1)} \mathbf{W}'_{(N-1)} + \frac{h}{4} \frac{h}{\mathbf{\Lambda}}_{(N)} \mathbf{W}'_{(N)}$$
(35)

For Eq. (32), lefting multiply both sides with

 $(\stackrel{+}{\boldsymbol{\Lambda}}_{(N)})^{\mathrm{T}}$ , and simplifying this equation with property 2 obtains

$$\left(\stackrel{+}{\boldsymbol{\Lambda}}_{(N)}\right)^{\mathrm{T}}\boldsymbol{\Lambda}_{(N)} - \frac{h}{4}\boldsymbol{W}_{(N)}' = \left(\stackrel{+}{\boldsymbol{\Lambda}}_{(N)}\right)^{\mathrm{T}}\boldsymbol{\mu}_{(N-1)} \quad (33)$$

where

$$\boldsymbol{\mu} = (\mu_1, \mu_2, \mu_3, \mu_0)^{\mathrm{T}} = \boldsymbol{\Lambda} + \frac{h}{4} \stackrel{+}{\boldsymbol{\Lambda}} \boldsymbol{W}' \qquad (34)$$

Exchanging the right side's order of Eq.(33) and simplifying the equation obtains

$$\begin{pmatrix} -\frac{h}{4}\boldsymbol{\omega}_{(N)}' \\ 1 \end{pmatrix} = \boldsymbol{U}_{(N-1)}\boldsymbol{\Lambda}_{(N)}$$
 (35)

where

$$U = \begin{pmatrix} -\mu_0 & -\mu_3 & \mu_2 & \mu_1 \\ \mu_3 & -\mu_0 & -\mu_1 & \mu_2 \\ -\mu_2 & \mu_1 & -\mu_0 & \mu_3 \\ \mu_1 & \mu_2 & \mu_3 & \mu_0 \end{pmatrix}$$
(36)

Thus

$$\boldsymbol{\Lambda}_{(N)} = \left(U_{(N-1)}\right)^{+} \begin{pmatrix} -\frac{h}{4}\boldsymbol{\omega}_{(N)}' \\ 1 \end{pmatrix} \tag{37}$$

where operator "+" denotes the matrix generalized inverse.

Substituting  $\Lambda$  into Eq.(18) gets the rotation matrix  $R_{4\times4}$ ; substituting  $R_{4\times4}$  and W' into Eq.(28) gets W; and substituting  $R_{4\times4}$  and W into Eq.(14) obtains the final solution algorithm.

According to the process, a flow chart is made to illustrate the procedure of the solution algorithm, as shown in Fig.3.

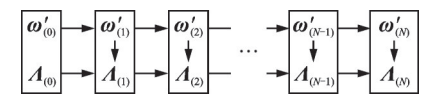


Fig.3 An open-loop process

### 3. 2 Virtual prototype verification

A virtual prototype is created, as shown in Fig.4. The inertial mass is a solid cube of which the side length is 40 mm, and the mass is 0.5 kg. The pedestal is a cubic enclosure of which the inner side length is 86 mm, and the outer side length is 90 mm. To improve simulation efficiency, the elastic limbs connecting the two components are simplified to springs with stiffness of  $5\times10^5~\text{N/m}$ . The fundamental excitements placed on the pedestal are

$$\begin{cases} a_{x} = -\frac{20\pi^{2}}{\sqrt{11}}\cos(10\pi t) + \frac{20\pi^{2}}{\sqrt{11}} \\ a_{y} = -\frac{180\pi^{2}}{\sqrt{11}}\cos(10\pi t) + \frac{180\pi^{2}}{\sqrt{11}} \\ a_{z} = -\frac{20\pi^{2}}{\sqrt{11}}\cos(10\pi t) + \frac{20\pi^{2}}{\sqrt{11}} \end{cases}$$
(38)

$$\begin{cases} \alpha_{x} = -\frac{375\pi^{3}}{3\sqrt{59}}\cos(10\pi t) + \frac{375\pi^{3}}{3\sqrt{59}} \\ \alpha_{y} = \frac{125\pi^{3}}{3\sqrt{59}}\cos(10\pi t) - \frac{125\pi^{3}}{3\sqrt{59}} \\ \alpha_{z} = \frac{875\pi^{3}}{3\sqrt{59}}\cos(10\pi t) - \frac{875\pi^{3}}{3\sqrt{59}} \end{cases}$$
(39)

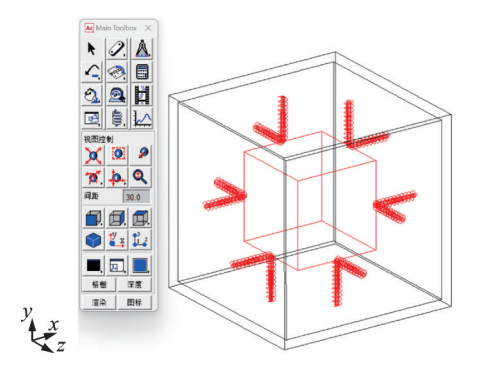


Fig.4 Virtual machine

The branch force data are measured through virtual prototype experiments, and acceleration data are obtained using the decoupling algorithm. A comparison between the efficiency of this solution algorithm and that of ADAMS is shown in Table 2. The result indicates that this solution algorithm is nearly five times faster than ADAMS.

Table 2 Solution efficiency of two algorithms

Running time	Algorithm used in	Algorithm proposed in		
Rulling time	ADAMS software	this paper		
τ/s	10.53	1.99		

Besides, these results are compared with the acceleration data measured in the virtual prototype experiments to determine the error rate of the decoupling algorithm. A comparison with the errors reported in Refs.[11-12] is shown in Table 3. The results indicate that the decoupling algorithm proposed in this paper performs better. However, this procedure may introduce small errors that may propagate throughout the data collection process.

Table 3 Error ratio of the virtual machine experiment
---

Time/s	9-limb type/%	12-limb type(in this paper)/ $\frac{9}{6}$
10	3.02	3.01
20	4.32	3.92
30	7.98	5.01
40	12.06	6.78
50	19.98	7.74
60	28.43	8.42

## 4 Auto-compensation

#### 4. 1 Auto-compensation strategy

There are truncation errors in the recursive process of the decoupling equations. Additionally, as observed in Fig.3, the recursive process for the decoupling equations is an open-loop process, and the error continuously accumulates throughout the recursive process. Therefore, an error auto-compensation algorithm is established to monitor and control the data during the decoupling process.

According to the vibration theory, vibrations are characterized by their periodic and continuous nature. Thus, when the dynamic equations are taken as its absolute value, the minimum value of the function is zero, which means

$$\mathbf{W} = (0.0.0.0)^{\mathrm{T}}$$
 (40)

$$\mathbf{\Lambda} = (0.0.0.1)^{\mathrm{T}} \tag{41}$$

where Eq. (40) corresponds to the case  $\langle 1 \rangle$ , here the angular velocity is zero, and Eq. (41) corresponds to the case  $\langle 2 \rangle$ , here the rotation angle is zero. Based on these two values, two observed feature values are established as

$$G_{\langle 1\rangle(N)} = \|\boldsymbol{W}'\|_2^2 \tag{42}$$

$$G_{\langle 2\rangle(N)} = \sum_{i=1}^{3} q_i^2 + (q_0 - 1)^2$$
 (43)

These two values are theoretically greater than or equal to zero. When the object's motion state corresponds to case  $\langle 1 \rangle$ , Eq.(42) equals zero, and when the motion state corresponds to case  $\langle 2 \rangle$ , Eq.(43) equals zero. However, due to the existence of errors, these two values probably do not equal zero in these cases. Therefore, a criterion is needed to determine which values should be compensated during the recursion process. The judgement criterion is

$$\begin{cases}
G_{\langle j\rangle(N)} < G_{\langle j\rangle(1)} \\
G_{\langle j\rangle(N)} < G_{\langle j\rangle(N-1)} & j = 1, 2 \\
G_{\langle j\rangle(N)} < G_{\langle j\rangle(N+1)}
\end{cases} (44)$$

The first equation indicates that the observed feature value is less than the set threshold, while the second and third equations indicate that the observed feature value is a local minimum of the function. If any judgement criteria is met, the compensation algorithm will adjust the value at that point to zero. To prevent a high misjudgement rate from an excessively large threshold or a high omission rate from an excessively small threshold, it is crucial to select an appropriate threshold. Here, the threshold is set to the first iterative value during the iteration process. This is because the first iterative value is close to zero. But due to the presence of iterative errors, this value will be greater than zero. The procedure of the decoupling algorithm with auto-compensation is shown in Fig.5.

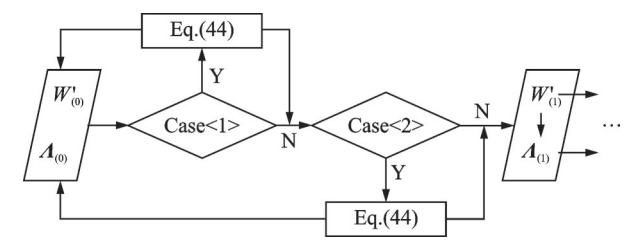


Fig.5 A semi-closed process

#### 4. 2 Virtual prototype verification

The same virtual prototype mentioned before is established to validate the effectiveness of the algorithm. The misjudgement rate and omission rate during the iteration process are shown in Table 4.

Table 4 Misjudgement rate and omission rate

1 able 4	Misjudgement rate and omission rate /0					
Noise	Misjudgement rate	Omission rate				
5	0	0				
10	0.5	1.0				
15	1.0	2.0				
20	1.5	2.5				
25	2.0	2.5				
30	2.0	3.5				
35	3.0	4.0				
40	4.0	4.5				

The results show that an increase in noise level positively affects both indicators, with higher noise leading to higher values for these indicators. However, even under significant noise interference, such as 40% noise, the algorithm maintains a low misjudgement rate and omission rate.

A comparison of error accumulations between the solution algorithm with auto-compensation and the one without it is made, as shown in Fig.6 and Fig.7.

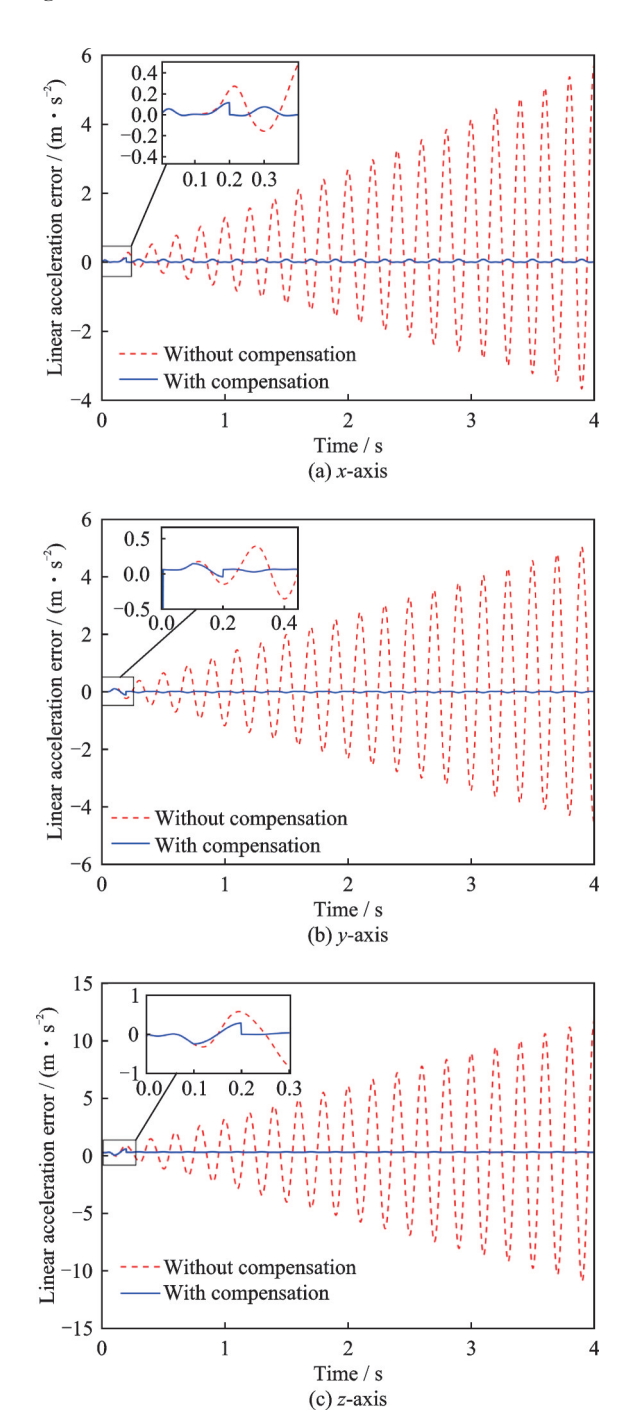
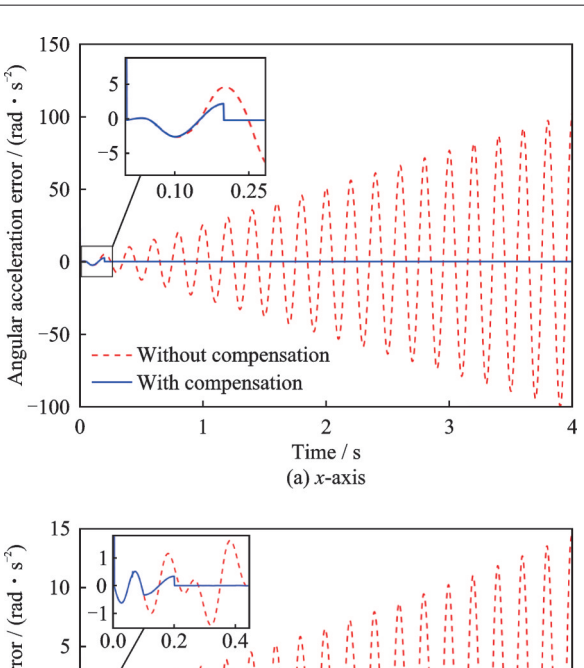
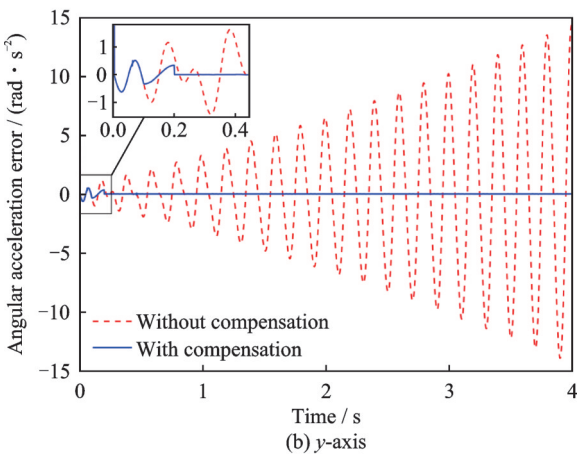


Fig.6 Error accumulations on linear accelerations





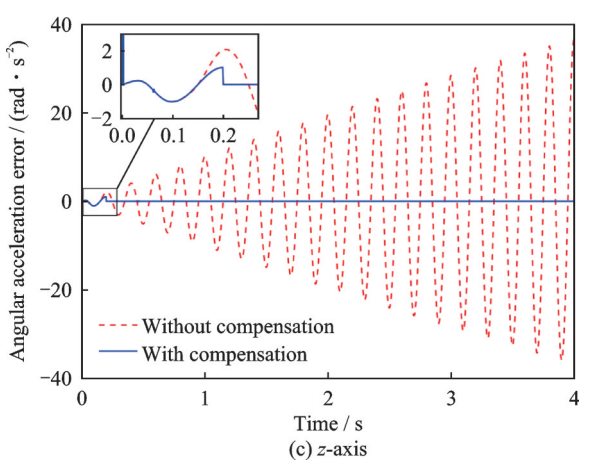


Fig.7 Error accumulations on angular accelerations

The result shows that with auto-compensation, the peaks of x-axis, y-axis, and z-axis linear accelerations are 12.293 6, 9.958 1, and 1.522 2 mm/s<sup>2</sup>, and the peaks of three axis angular accelerations are 0.008 7, 0.011 1, and 0.005 0 rad/s<sup>2</sup>, respectively. After compensation, the error converges, while the error without compensation diverges, indicating the decoupling algorithm with auto-compensation is effective.

### 5 Conclusions

- (1) Based on Kane's method, the dynamic model is established. Kane's method is well suited for acceleration decoupling processes due to several advantages, including introducing small amounts of variables and equations and employing low-order differential equations and the needlessness of force analysis.
- (2) With the trapezoidal rule, the dynamic equations are solved, and virtual prototype experiments are conducted. The results show that the solution efficiency of this algorithm is approximately five times higher than that of the ADAMS core algorithm. Additionally, when the algorithm is applied to the "12-6" configuration and the "9-3" configuration, the solution efficiency of the former is about 3.3 times that of the latter.
- (3) Based on the vibration theory, an auto-compensation algorithm is proposed and tested through simulations. The results indicate that with increasing noise interference, the misjudgement rate and the omission rate also increase. Under 40% noise interference, these two indices are only 4.0% and 4.5%, respectively. Moreover, during the recursive solving process of the six accelerations, the solving errors converge.

#### References

- [1] CHEN L, SUN H X, ZHAO W, et al. Robotic arm control system based on AI wearable acceleration sensor[J]. Mathematical Problems in Engineering, 2021, 2021: 5544375.
- [2] ZHAO P, ZHOU Y F. Active vibration control of flexible-joint manipulators using accelerometers[J]. Industrial Robot: The International Journal of Robotics Research and Application, 2019, 47(1): 33-44.
- [3] HE HY, ZHAF, LIF, et al. A combination scheme of pure strapdown and dual-axis rotation inertial navigation systems[J]. Sensors, 2023, 23(6): 3091.
- [4] YU D L, LV Z Y, ZHANG K T. Research on second order complementary filter strapdown inertial navigation algorithm based on information fusion[C]//Proceedings of the 3rd International Conference on Sensors and Information Technology (ICSI 2023). Xiamen, China: SPIE, 2023.
- [5] WANG N. Satellite/inertial navigation integrated navi-

- gation method based on improved Kalman filtering algorithm[J]. Mobile Information Systems, 2022, 2022; 4627111.
- [6] SUN C Y, LI K. A positioning accuracy improvement method by couple RINSs information fusion[J]. IEEE Sensors Journal, 2021, 21(17): 19351-19361.
- [7] LYU D H, WANG J Q, HE Z M, et al. Landmark-based inertial navigation system for autonomous navigation of missile platform[J]. Sensors, 2020, 20(11): 3083.
- [8] WANG D H, YUAN G. A six-degree-of-freedom acceleration sensing method based on six coplanar single-axis accelerometers[J]. IEEE Transactions on Instrumentation and Measurement, 2011, 60(4): 1433-1442.
- [9] YOU Jingjing, LI Chenggang, WU Hongtao, et al. Hybrid decoupling algorithm and error auto-compensation algorithm of the parallel type six-axis accelerometer[J]. Chinese Journal of Scientific Instrument, 2015, 36(10): 2249-2257. (in Chinese)
- [10] YOU Jingjing, LI Chenggang, WU Hongtao, et al. Research on the decoupling algorithm of pre-stressed parallel six-axis accelerometer[J]. Chinese Journal of Scientific Instrument, 2017, 38(5): 1216-1225. (in Chinese)
- [11] YOU Jingjing, LI Chenggang, WU Hongtao. Research on the design and modelling of a six-axis acceleration sensor based on a parallel mechanism[J]. Journal of Vibration Engineering, 2012, 25(6): 658-666. (in Chinese)
- [12] YOU J J, LI C G, WU H T. Research on Hamiltonian dynamics of parallel type six-axis accelerometer[J]. Journal of Mechanical Engineering, 2012, 48(15): 9-17.

**Acknowledgements** This work was supported by the Opening Project of State Key Laboratory of Mechanical Transmission for Advanced Equipment (No.SKLMT-MSKFKT-202330), the National Natural Science Foundation of China (NSFC) (No.52575022), and the Postgraduate Research & Practice Innovation Program of Jiangsu Province (No. KYCX24\_1295).

#### Authors

The first author Ms. ZHANG Yuanwei received her B.S. degree in mechanical engineering from Zhejiang University of Science and Technology, Zhejiang, China, in 2023. She is currently purchasing her M.S. degree in Nanjing Forestry University, Nanjing, China. Her research interest is statics and dynamics of six-axis acceleration sensing mechanisms.

The corresponding author Prof. YOU Jingjing received

his B. S. degree from Nanjing Forestry University in 2007, M. S. and Ph. D. degrees from Nanjing University of Aeronautics and Astronautics in 2010 and 2013, Nanjing, China, respectively. He has worked as professor with Nanjing Forestry University since 2018. His research interest is focused on parallel robot mechanism.

**Author contributions** Ms. ZHANG Yuanwei proposed the idea of auto-compensation algorithm, conducted the

virtual experiments and wrote the manuscript. Prof. YOU Jingjing designed the mechanisms and supervised the experiments and writing. Mr. ZHANG Xianzhu processed the data. Mr. SHI Haofei derived the dynamic model. All authors commented on the manuscript draft and approved the submission.

**Competing interests** The authors declare no competing interests.

(Production Editor: XU Chengting)

# 六轴加速度感知机构解耦算法

张缘为,尤晶晶,张显著,史浩飞(南京林业大学机械电子工程学院,南京 210037,中国)

摘要:针对现有的六轴加速度解耦算法求解低效、精度不高的问题,提出了一种新的解耦算法及误差自补偿算法。首先,基于凯恩方法建立了六轴加速度传感器的动力学模型,并确定了支链力与加速度之间的关系。然后,根据梯形公式构建了动力学方程的求解算法。虚拟样机实验表明,该算法的计算效率比ADAMS核心算法高5倍。此外,将算法分别应用于"12-6"构型和"9-3"构型上,前者的计算效率约为后者的3.3倍。最后,基于振动理论构建了一种适用于该求解算法的自补偿算法。虚拟样机实验表明,在40%的噪声影响下,该自补偿算法的误判率和漏判率分别为4.0%和4.5%,同时误差收敛。

关键词: 六轴加速度感知机构; 凯恩方法; 梯形公式; 自补偿